ENGINEERING

Sound-controlled fluidic processor

Hengjia Zhu[1], Qiyu Deng[1], Junzhi Li[2], Ling Yang[1], Hegeng Li[1], Zhipeng Zhao[1], Zuochen Wang[1], Chunlin Pang[1], Yiyuan Zhang[3], Vincent Chi-Hang Lui[2], Wei Li[1,4]*, Xiaobo Yin[1]*, Liqiu Wang[3]*

Copyright © 2025 The Authors, some rights reserved; exclusive licensee American Association for the Advancement of Science. No claim to original U.S. Government Works. Distributed under a Creative Commons Attribution NonCommercial License 4.0 (CC BY-NC).

Precision processing of various liquids while maintaining their purity holds immense potential for many applications. However, liquids tend to leave residues that contaminate handling tools and compromise volumetric precision, necessitating contactless strategies to prevent liquid loss. Biological and chemical samples carried by fluids can be sensitive to physical stimuli, demanding mild but effective means to preserve integrity. Here, we report a sound-controlled fluidic processor for complete and well-controlled microfluidic functions, including moving, merging, mixing, and cleaving, in contactless and harmless manners. The processor generates an acoustophoretic force field that serves as a versatile toolbox for manipulating droplets with surface tension from 17.9 to 72 millinewtons per meter and volume from 1 nanoliter to 3 milliliters, offering a wealth of operations crucial to fundamental biomedical and chemical practices.

INTRODUCTION

Well-controlled processing of fluids in a highly adaptive manner becomes substantial in many thermal, optical, electrical, and biomedical fields (*1*–*11*). For example, to detect severe acute respiratory syndrome coronavirus 2, the diagnostic specialists need to extract viral RNA from the swabs, then amplify, and quantify the genetic material using quantitative polymerase chain reaction—completing a whole series of fluidic operations in microliters of fluid media. For any of these operations, preserving fluids' material purity and volumetric precision is critical. Delicate control of physical fields, including light, magnetism, heat, and electricity, offers contactless solutions to avoid such liquid loss and cross-contamination (*12*–*16*). However, they suffer from overwhelming field strength and stringent temperature that may damage chemicals or biological samples carried by the fluid, demanding a clean, mild, but effective method for fluidic operation (*17*). Acoustic stimulus, as intrinsically mechanical wave, has been a promising alternative due to high-level biocompatibility, high-precision controllability, and cost-effectiveness (*18*–*21*). The unprecedented progress in standing wave–based acoustic microfluidics embraces these merits, including surface acoustic wave (SAW) (*5*, *22*), bulk acoustic wave (BAW) (*23*, *24*), acoustic levitation (*6*, *25*, *26*), and focal point trapping (*27*), where the spatiotemporal control of local Gor'kov potential minimum attracts droplets and objects. SAW and BAW techniques control droplets using acoustic waves propagating along the surface or through the bulk of a piezoelectric material, while acoustic levitation and focal point trapping rely on the rigorous modulation of standing waves. These methods enrich the toolbox for droplet manipulation in both liquids and air. However, the acoustic splitting of droplets in a controllable manner remains challenging, as it requires sufficient diverging forces to overcome surface tensions. Precisely engineered Gor'kov potentials drive droplet splitting in combination with acoustic streaming in oil, while in air, they induce out-of-plane ejection to achieve droplet division (*28*, *29*). Nevertheless, the specially engineered piezoelectric materials and surfaces compromise the tuning of acoustic radiation force field for versatile fluidic operations. Moreover, they only work for a narrow range of liquid types and volumes (in the scale from hundreds of nanoliters to tenth of microliters). To date, the acoustic manipulation of liquids, including separating, pushing, pulling, merging, and vortexing, for a variety of liquid types and volumes, remains challenging.

Here, we present a sound-controlled fluidic processor (SFP) to enable a full landscape of fluidic operations of diverse liquids with surface tensions from 17.9 to 72.0 mN m^{-1} and volumes from 1 nl to 3000 μl in a contactless and damage-free manner. The SFP consists of an acoustic transducer and a slippery surface, whose spatial relationship creates tunable acoustophoretic force fields, yielding pushing or pulling forces to move, merge, split, and mix droplets on demand. The flexibility of the SFP enables various tasks, including colorimetric reactions, precipitation reactions, and biodetection, on flat, curved, and even complex substrates made of metals, glass, and polymers. This merit further extends to fundamental biological applications, where mouse primary liver organoids are cultured and screened for drugs including verapamil and biliatresone. Our microfluidic strategy is, thus, highly potent for wide applications such as lab-on-a-chip systems, droplet-based manufacturing, and microassays, to name a few.

RESULTS

Design of the SFP

The SFP platform consists of a 58-kHz ultrasonic source (fig. S1) and a highly adaptable slippery surface (Fig. 1A and figs. S2 and S3). On the prepared slippery surfaces, liquids, with surface tensions spanning from 17.9 to 72.0 mN m^{-1}, move readily at low sliding angles (≤5°) (fig. S3). The oil-infused nature endows the slippery surface with self-repairing and pressure-stable omniphobicity (*30*) and, thus, enhances robustness toward abrasions (fig. S3). This design is effective for liquids that are immiscible with slippery oil and works for a variety of substrates with complex geometries, including metals, glass, and polymers (*31*, *32*).

In contrast to the limited microfluidic functionalities of potential well that can only move or merge microliter droplets (*33*), the synergetic effort of the acoustic stimuli and the slippery surface generates an acoustophoretic force field, endowing the SFP with stability

Downloaded from https://www.science.org at Hong Kong Polytechnic University on June 23, 2025

---

[1]Department of Mechanical Engineering, The University of Hong Kong, Hong Kong SAR 999077, P.R. China. [2]Department of Surgery, The University of Hong Kong, Hong Kong SAR 999077, P.R. China. [3]Department of Mechanical Engineering, The Hong Kong Polytechnic University, Hong Kong SAR 999077, P.R. China. [4]School of Biomedical Sciences, The University of Hong Kong, Hong Kong SAR, 999077, P.R. China.
*Corresponding author. Email: liqiu.wang@polyu.edu.hk (L.W.); xbyin@hku.hk (X.Y.); weli@connect.hku.hk (W.L.)

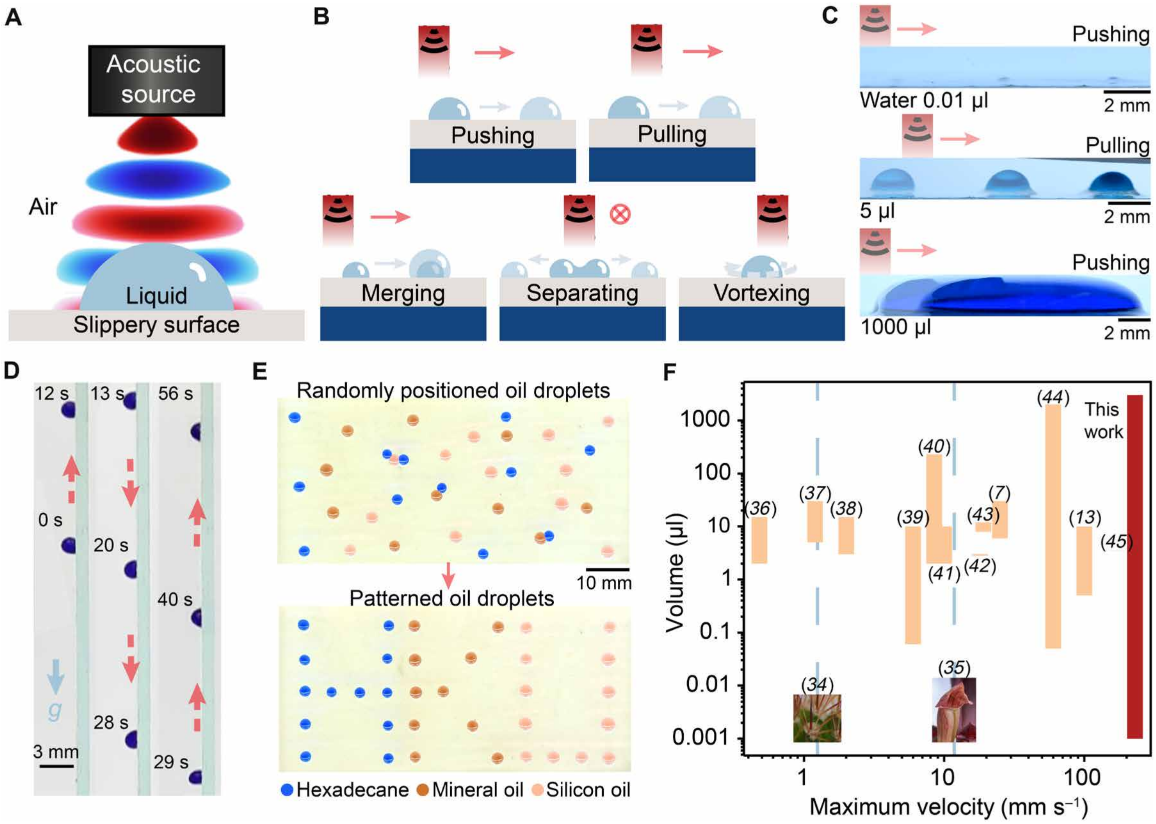

Fig. 1. Design and demonstration of the SFP. (**A**) Schematic of the SFP. The acoustic wave generated by the acoustic source in air drives liquid droplet motion on a slippery surface. (**B**) Schematics of droplet manipulation by the SFP, including pushing, pulling, merging, separating, and vortexing. The gray-blue arrows indicate the moving direction of the droplets, while the red arrows indicate the moving direction of the acoustic source. The red gradients with black curved lines indicate the acoustic field. (**C**) Chronophotographs showing acoustic manipulation of water droplets with different volumes. Here, the SFP pushes a 0.01-μl water droplet and a 1000-μl water puddle and pulls a 5-μl water droplet. (**D**) Chronophotographs showing manipulation of a 2.5-μl blue-dyed water droplet on a vertical slippery surface. The dashed red arrows indicate acoustic source and droplet moving directions, and the light blue arrow indicates the direction of gravity. (**E**) Sequential images showing on-demand patterning of randomly positioned oil droplets, including hexadecane (blue), mineral oil (brown), and silicon oil (pink). The droplets are dispensed onto the slippery surface together and then repositioned into a pattern of letters "H," "K," and "U," using the SFP. (**F**) Droplet manipulation performance comparison with other techniques in terms of maximum velocity versus controllable volume range. Image credit: W.L. and H.Z., The University of Hong Kong.

and controllability to perform rich microfluidic functionalities, including separating and vortexing, in addition to moving and merging while breaking the volume limitation (Fig. 1, B and C). The air-liquid interface scatters and absorbs the ultrasound, which generates acoustophoretic force to drive droplets into motion with minimal damage to the carrying substances (fig. S4). Besides horizontal droplet maneuvering on a downward-facing surface (fig. S5 and movie S1), the SFP can remarkably transport a droplet on the vertically placed slippery surface either upward or downward (Fig. 1D and movie S2). The precision patterning of random low–surface tension oil droplets (Fig. 1E and movie S3) is also achievable on slippery surfaces. Compared with other manipulation strategies on natural surfaces (*34*, *35*) or on engineered surfaces (*7*, *13*, *36*–*45*), the SFP shows a high transportation speed of 23 cm s^{-1} (fig. S6 and movie S4) and large working volume range across six magnitudes (from nanoliters to milliliters), showing enhanced performance for robust and versatile liquid operations (Fig. 1F).

A full landscape of fluidic operations

Embracing the merits of acoustic tweezers and beyond, the SFP also acts as an acoustic blade to cut fluids, enabling a full landscape of fluidic operations, including pulling-based navigation and merging, as well as pushing-based navigation, separation, and merging (Fig. 2A). The SFP generates a stable acoustic field that can trap and move a 2.5-μl droplet for a long distance (~65 mm) in a well-controlled manner (Fig. 2B and movie S5). The droplet stabilizes around 3.5 mm away from the acoustic source center, closely resembling the behavior of acoustic trapping by Gor'kov potential minimum (*5*, *46*). The versatility of the acoustic field extends to liquids with various volumes and types (Fig. 2, C and D). When manipulating milliliter liquids, the acoustic field creates a notch on the liquid puddle, producing a pushing force to drive it into motion (Fig. 2C and movie S5). The SFP can also manipulate nanoliter droplets by pushing or pulling forces (Fig. 2D and movie S5); for example, it pulls two 1-nl silicon oil droplets across more than 20 times the droplet diameter. In addition to silicone oil droplets (surface tension being 17.9 mN m^{-1}), our platform can also control water droplets (surface tension being 72.0 mN m^{-1}) with volume ranging from 5 nl to 3 ml (fig. S7 and movie S6). Together with programmable droplet motion along a desired path (Fig. 2E and movie S5), such a wide range of liquid types and volumes endow SFP with capabilities toward precision microfluidic manipulations for various applications.

Downloaded from https://www.science.org at Hong Kong Polytechnic University on June 23, 2025

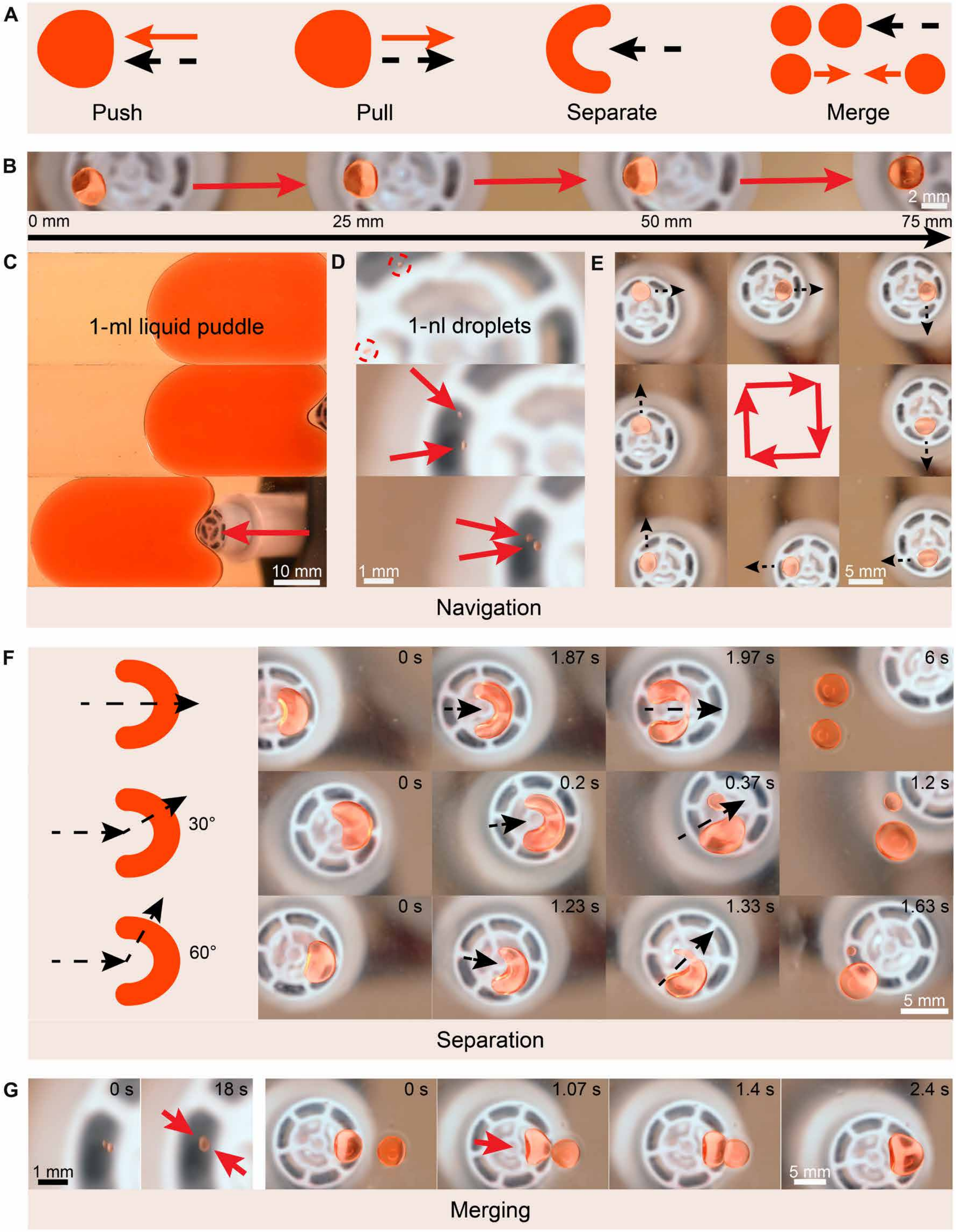

Fig. 2. Liquid operations based on the SFP. (**A**) Schematics demonstrating navigation (pushing and pulling), separation, and merging operations based on the SFP. The red arrows represent droplet motion direction, while the dashed black arrows represent acoustic source motion direction. (**B** to **G**) Operation of silicon oil droplets dyed by oil red. (B) Chronophotographs showing long-distance (~65 mm) pulling of a 2.5-μl droplet. (C) Sequential images showing pushing of a 1-ml puddle. (D) Sequential images showing pulling of two ~1-nl droplets. The dashed red circles indicate the initial positions of ~1-nl droplets. (E) Sequential images showing pushing of a 2.5-μl droplet along a square path. (F) Schematics and sequential images showing controlled separation of a 10-μl droplet, where the separation process begins with droplet deformed to a "U" shape and the motion direction of the acoustic source determines the separation volume. (G) Sequential images showing fusion of two silicon oil droplets influenced by pulling (left) and pushing (right). Image credit: H.Z., The University of Hong Kong.

Downloaded from https://www.science.org at Hong Kong Polytechnic University on June 23, 2025

Different from separating two closely placed solid objects, separation of liquid generally requires forces with opposite directions sufficient to overcome surface tension. State-of-the-art advancements in acoustic microfluidic have used SAW to split droplets (*28*, *29*). In contrast, on the SFP platform, delicate control of acoustic radiation force distribution on the droplet enables readily separation of the droplet. The acoustic radiation force deforms the droplet to "U" shape (Fig. 2F and movie S7). Tuning the acoustic source motion direction further divides the U-shaped droplet into two portions with desired volumes, enabling splitting and dispensing of the droplets on demand and outperforming previous methods based on acoustic trapping or suspension (*27*, *33*). Pushing or pulling also enables reverse operation, i.e., merging (Fig. 2G and movies S5 and S7). These merits both as a tweezer and as a blade, in a well-controlled manner, offer robust and versatile fluidic operations that have not been reported before.

Working mechanism

To understand the underlying mechanisms of the SFP platform, we study the behavior of a 10-μl dodecane droplet placed 2.7 mm under an upright positioned acoustic source (Fig. 3A, fig. S8A, and movie S8). Changing the spatial relationship between the acoustic source and the droplet can achieve pushing, separating, and pulling of droplets (Fig. 3A). The droplet experiences a pushing acoustic force as it moves at the front of the center of the acoustic source, while the droplet experiences a pulling acoustic force as it is trapped and moves behind the center of the acoustic source. The droplet splits into two parts as the center of the acoustic source passes over it. The net force F_{net} responsible for droplet movement is the resultant from the radial component of the acoustic radiation force $F_{\mathrm{ar,r}}$ and viscous force F_{η}: $F_{\mathrm{net}} = F_{\mathrm{ar,r}} - F_{\eta}$ (for more details, please see Supplementary Text and fig. S9).

To further understand this distinct droplet behavior, we simulate the acoustic pressure and force distribution on the droplet based on the spatial relation among acoustic source, the surface, and the droplet: acoustic source center to droplet center distance D and acoustic source center to slippery surface (i.e., droplet bottom) distance H. The finite element analysis simulation model contains three elements: a cuboid representing the SFP working space, an acoustic source with the exact emission structure of a 58-kHz ultrasonic sensor, and a droplet modelled using a spheric fit to closely resemble its actual morphology (fig. S10). Corresponding to the actual droplet motions, at three typical positions during manipulation, we evaluate the acoustic pressure distribution on the surface and the droplet along with acoustic radiation force distribution on the droplet surface (Fig. 3, B and C, and fig. S8, B to D). The addition of a droplet away from the acoustic beam center disrupts the center symmetry of the acoustic pressure distribution (Fig. 3B and fig. S11A), resulting in a unidirectional net force along the radial axis. The interaction with the acoustic field also changes the pressure distribution on the droplet surface, suggesting morphological change of the droplet (Fig. 3C). During pushing ($D = 0.3$ mm), the stronger force magnitude near the droplet apex results in a shifted triangular projection on the side view.

Downloaded from https://www.science.org at Hong Kong Polytechnic University on June 23, 2025

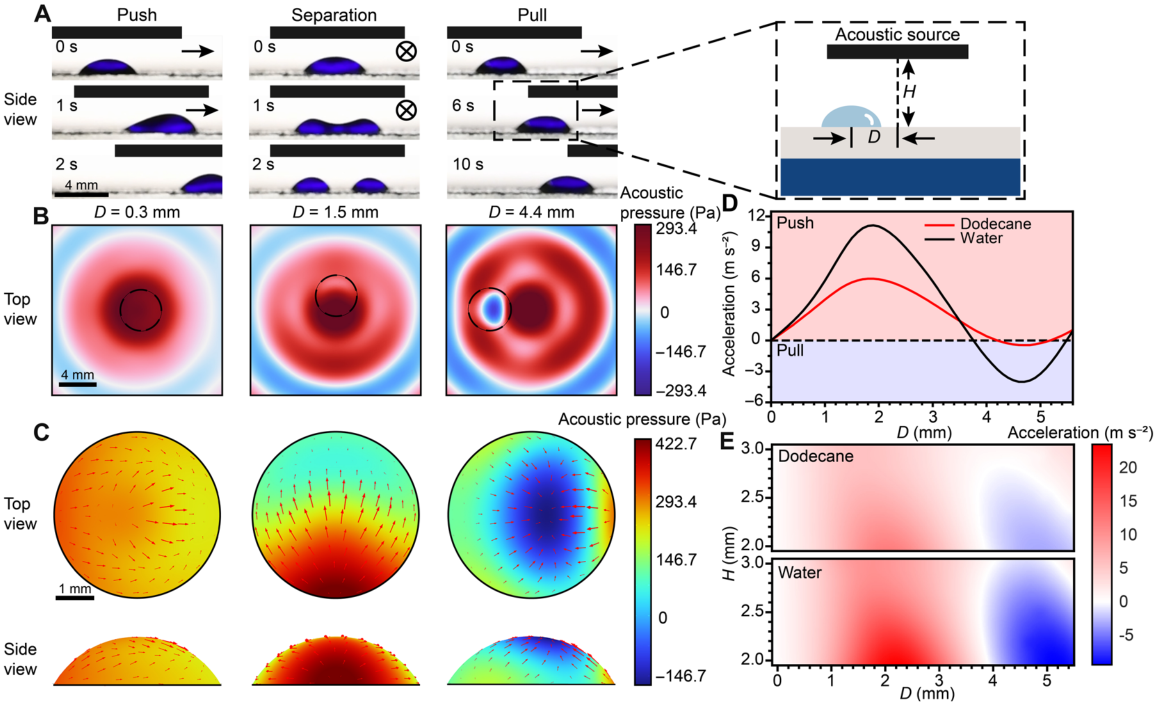

Fig. 3. Working mechanism of the SFP. (**A**) Three typical manipulation modes of the SFP presented by a 10-μl dodecane droplet. We defined the manipulation modes by two parameters: acoustic source center to droplet center distance D and acoustic source center to slippery surface distance H. The black arrows and circles with crosses indicate the movement direction of the acoustic source. (**B**) Top view of acoustic pressure distribution on the slippery surface and the dodecane droplet at three typical manipulation positions ($D = 0.3$, 1.5, and 4.4 mm) at $H = 2.7$ mm. (**C**) Top and side view of the acoustic pressure and force distribution on the droplet surface at the corresponding manipulation positions. The direction and the length of red arrows represent the force direction and relative amplitude. (**D**) Net acoustic acceleration in droplets' motion direction integrated over the surfaces of a 10-μl dodecane droplet and a 10-μl water droplet placed at $H = 2.7$ mm with respect to D. The positive acceleration values (red) represent pushing of the droplet, and the negative values (blue) represent pulling of the droplet. (**E**) The net acoustic acceleration of a droplet is determined by the position relative to the acoustic source, namely, D and H. Image credit: H.Z., The University of Hong Kong.

During separation ($D = 1.5$ mm), the wide force distribution range, together with the aid of viscous force, breaks the original shape of the droplet. The large expelling force near acoustic source center functions as a blade that provides sufficient acoustic radiation force to overcome surface tension (Fig. 2F). During pulling ($D = 4.4$ mm), the acoustic source acts on the apex of the droplet with negative pressure, creating a local minimum near the source. This force distribution results in the dome-shaped droplet during transportation. Because of smaller surface force magnitude, the deformation of the droplet is not as obvious as that during the pushing mode.

We further evaluate the influence of the acoustic interaction on droplet motion by integrating the acceleration component along the motion axis over the droplet surface. To approximate the actual value of the acceleration, we simulate a model of the droplet resting on a vertically placed surface (fig. S12), where the bulk droplet experiences a net force balance of gravitational force F_g, viscous force F_η, and vertical component of acoustic radiation force $F_{ar,v}$: $F_g + F_\eta = F_{ar,v}$. As a result, under the same acoustic field (i.e., same H), the damping sinusoidal acceleration curve is consistent with experimental phenomena (Fig. 3D). Comparing net acceleration between dodecane and water further illustrates the morphological effect, where, under the same liquid volume, liquid with higher contact angle experiences a larger acoustic acceleration (fig. S11, B and C). The variation of H exhibits monotonic change within half ultrasonic wavelength, where closer acoustic source position to the surface would generate larger actuation force on the droplet (Fig. 3E). The variation of the droplet volume from nanoliter to microliter induces shifting of the pulling and pushing positions and relative acoustic acceleration magnitude through simulation (figs. S13 and S14). When the distance between the transducer and the droplet is less than 0.2 mm, the pressure field may cause cavitation effects at the air-liquid interface (*47*).

Acoustic vortexing and versatility

The interaction between the acoustic field and the droplet induces acoustic streaming effect in the droplet (*48*), generating vortices that facilitate conductive mixing. To explore the acoustic vortexing effect, we conduct numerical simulations and visual demonstrations of the flow field in a 200-μl water droplet merged with a 5-μl dyed water droplet (Fig. 4, A to C, and movie S9). The simulated flow line profile, from an acoustic source placed at $D = 7.6$ mm, $H = 2.7$ mm, and tilted 45°, indicates that the strongest fluid shear occurs near the surface with highest acoustic pressure (Fig. 4A). The projected cross-sectional views at the high acoustic pressure region of this model offer reliable predictions of internal flow within the droplet during acoustic vortexing, confirmed by the mixing experiment (Fig. 4B and movie S9). Careful control of the acoustic source motion generates a macroscale vortex pattern. Compared to diffusive mixing, from the top view, the acoustic vortexing offers much faster and more uniform mixing in the droplet (Fig. 4C).

The enhanced mixing performance extends the potential of the SFP beyond simple merging functions. Such a robust and versatile maneuvering strategy ensures the SFP as a reliable platform for desired microfluidic operations. SAW and BAW devices have extensively facilitated the study of acoustic vortexing, relying on specially designed piezoelectric substrates and advanced nanofabrication techniques (*5*, *22*, *23*, *28*). These technologies enable precise placement and vortexing of particles in fluid media ranging from nanometers to millimeters. In contrast, the SFP offers greater flexibility in microfluidic device design and material selection, enabling versatile and efficient mixing and vortexing of droplets for a variety of application scenarios. As demonstration, we use a colorimetric chemical detection method utilizing thymol blue to monitor the acid-base reaction involving a 10-μl 1 M potassium hydroxide droplet and a 9-μl 1 M hydrochloride droplet on a copper substrate (Fig. 4D). Mixing the potassium hydroxide droplet with the indicator at first changes its color from red to dark blue. After combination with the hydrochloride droplet, the mixture presents a blend of red and blue colors. Without vortexing, the droplet exhibits a dominating red color; however, after sufficiently mixed with acoustic vortexing, the droplet presents a dark blue color, consistent with higher base contents in the precursors (movie S10). Moreover, the conformability of the slippery layer allows for manipulation on curved polylactic acid surface fabricated via 3D printing including transportation, merging, and vortexing (fig. S15 and movie S11).

The immiscible nature of the lubricant oil with common solvents and reagents endows lossless and antifouling capabilities to sustainably support a variety of chemicals reactions and detections. For example, strong pollutants, two droplets of saturated iodine in 5% (w/v) NaOH solution, react with a 1 M hydrochloride droplet and an acetone droplet, a low–surface tension solvent, on a nitrile rubber–based substrate (Fig. 4E and movie S12). Following microfluidic maneuvering of those droplets, sufficient acoustic vortexing ensures iodine precipitation and iodoform generation with high uniformity. Moreover, the SFP can conduct precipitation reaction of iron(III) chloride and potassium hydroxide on a glass substrate, evenly distributing the precipitation within the droplet without any staining on the surface during transportation and vortexing (fig. S16 and movie S13). Advancing beyond single transducer limit, the integration of a motion stage and multiple acoustic sources enables automatic parallel screening with precise spatiotemporal control (fig. S17 and movie S14). As a practical demonstration, we apply this system to Griess test of daily water samples to detect whether nitrite salt levels fall within a safe range. Therefore, our technique interacts with fluids in a contactless and loss-free manner and works for a wide variety of biomedical/chemical reactions and analyses in an automated and scalable way.

Biodetection and organoid culturing

Demonstrating antifouling, lossless, and precise operation capabilities, the SFP may extend to fundamental biomedical applications, where cross-contamination and volumetric imprecision caused by residues on the operating tools are a key concern. On the other hand, incorporation of lossless liquid manipulation strategy into current bioassay practices remains challenging since the durability of the surface hinders long-term experiments (*49*). To test SFP's feasibility, we perform colorimetric analysis of biomarkers and reagents (Fig. 5A). As a demonstration, we use the SFP to detect bovine albumin droplets with different concentrations with 5-μl biuret reagent droplets, which are dispensed from a 20-μl reservoir with the aid of a separation barrier. After sufficient vortexing, copper(II) ions form coordination complexes with peptides. The higher the peptide concentration, the more purple color appears (Fig. 5B and movie S15), which is even observable at low concentrations. To demonstrate the biocompatibility and long-term function of the SFP, we culture the liver organoids for 7 days in Matrigel with mouse primary cholangiocytes, a type of epithelial cells in bile ducts, exhibiting cell viability higher than 95% with no statistical difference from those cultured on a biocompatible polydimethylsiloxane (PDMS) substrate (fig. S18).

Downloaded from https://www.science.org at Hong Kong Polytechnic University on June 23, 2025

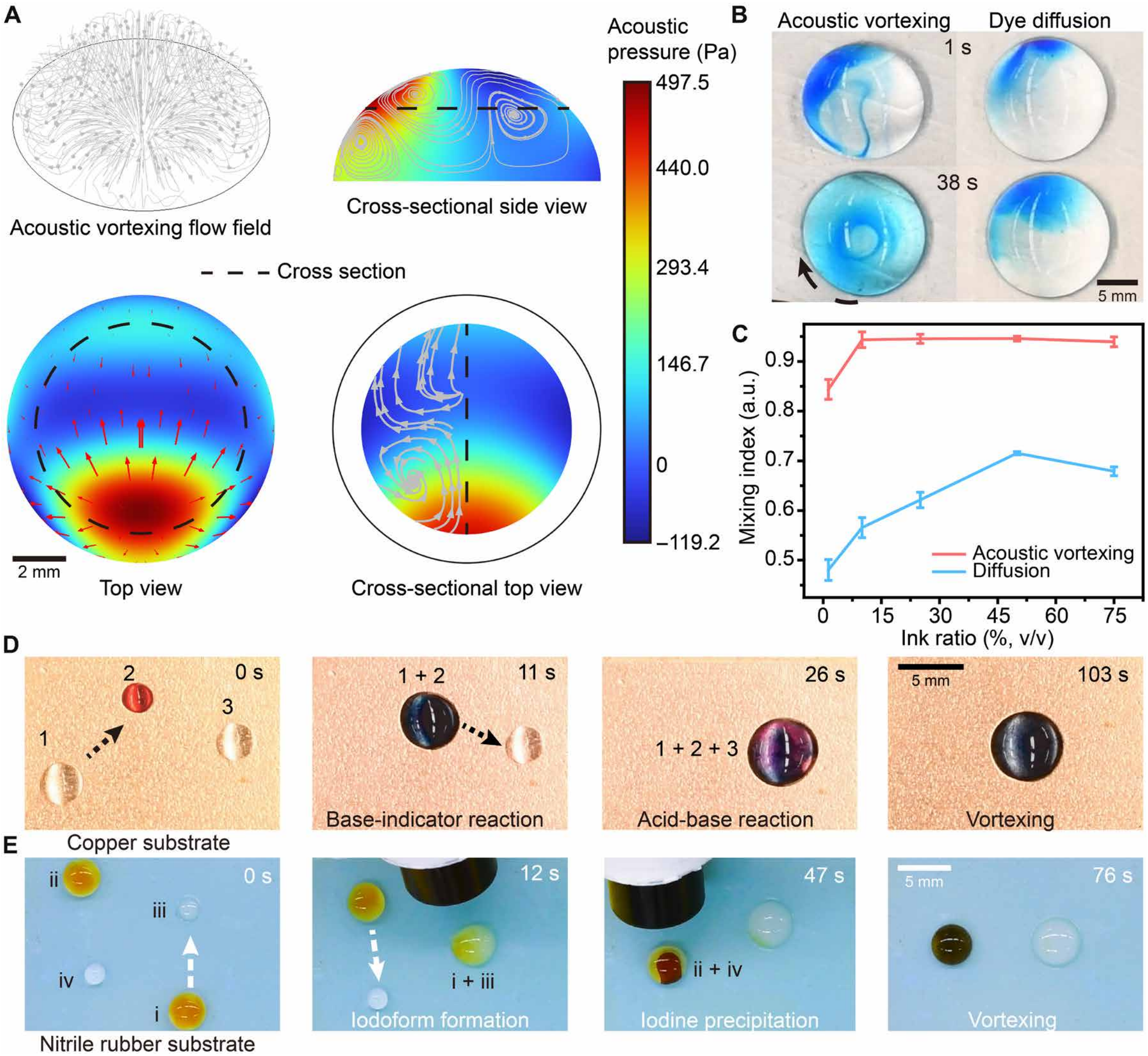

Fig. 4. Acoustic vortexing and versatility of the SFP. (**A**) Simulation of flow field, acoustic pressure distribution, and force distribution in a 200-μl water droplet placed at $H = 2.7$ mm and $D = 7.6$ mm relative to acoustic source tilted 45°. The gray lines with arrows indicate the flow direction, the red arrows indicate the surface force direction, and their lengths indicate relative magnitude. (**B**) Sequential images demonstrating flow field by acoustic vortexing and diffusion of a 200-μl water droplet merged with a 5-μl blue-dyed water droplet. The dashed black arrow represents the moving direction of the acoustic source. (**C**) Acoustic vortexing facilitates accelerated mixing performance compared to diffusion. Here, combinations of blue-dyed ink droplets and water droplets, adding up to 200 μl, are mixed simultaneously using acoustic vortexing and diffusion. After the completion of acoustic vortexing, we measure the mixing index, which is defined as one minus the ratio of the SD of the gray values within the droplet after and before mixing. a.u., arbitrary units. (**D** and **E**) Versatile chemical reactions performed by the SFP on various substrates of choice. The dashed arrows indicate droplet motion directions. (D) Sequential images showing acoustic vortexing of a potassium hydroxide droplet 1 with a thymol blue droplet 2 and then a hydrochloride droplet 3 on a copper substrate. (E) Sequential images showing acoustic vortexing of iodine saturated solution in 5% (w/v) sodium hydroxide on a nitrile rubber substrate with sodium hydroxide droplets i and ii. The precursor droplets react with acetone droplet iii and HCl droplet iv to form iodoform suspension and iodine precipitation, respectively. Image credit: H.Z., The University of Hong Kong.

Conventional organoid culture methods seed cells in a biological matrix within microwells or hanging drops, providing a 3D biomimetic environment that supports self-organization and physiological function. However, matrix removal can damage organoids and increase contamination risks, compromising their integrity and reliability for organoid-based assays (*50*, *51*). Along with the damage-free capability, scalability, and long-term stability, the SFP may be integrated into a lab-on-a-chip system, enabling the culture and analysis of cells and organoids on a single platform. The SFP provides a damage-free, contamination-free, and effective solution for both organoid culture and drug screening, streamlining complex experimental processes. As proof of the concept, we culture the liver organoids, release them with cold medium, add drug and immunofluorescent stains to them, and lastly observe them using confocal imaging (Fig. 5C). To test the functions of the liver organoids cultured on the SFP, we measure their efflux capability using rhodamine 123, a fluorescent dye that can be transported by multidrug resistance protein 1 (MDR1) of bile duct cells (*52*). We compare the transportation behavior of liver organoids with 10 μM verapamil-treated liver organoids, where both are placed under ambient conditions for rhodamine 123 efflux experiment (Fig. 5D

Downloaded from https://www.science.org at Hong Kong Polytechnic University on June 23, 2025

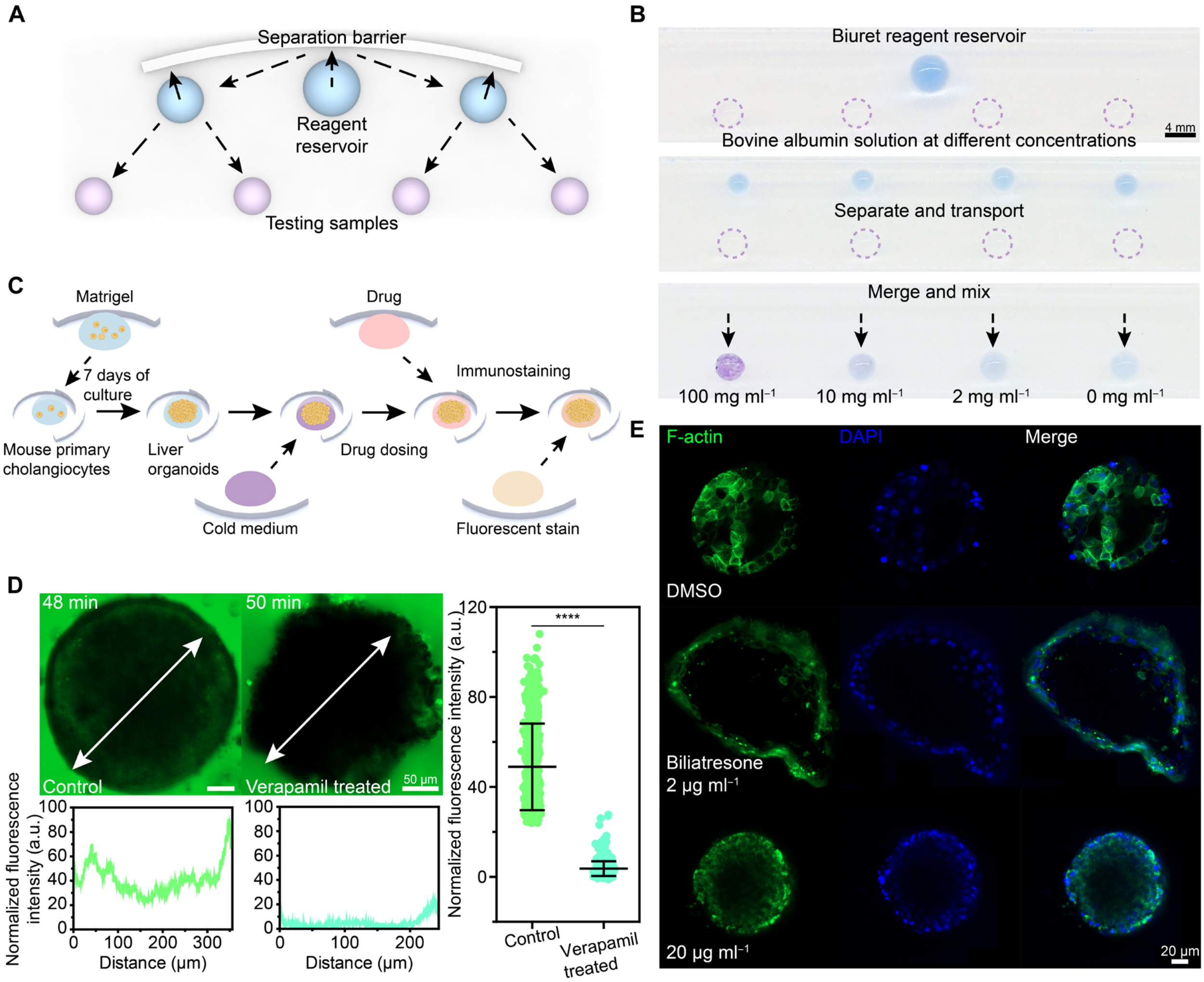

Fig. 5. Biodetection and organoid screening with the SFP. (**A** and **B**) Schematic diagram and sequential images demonstrating protein detection via on-demand separation of biuret reagent, a high surface tension fluid, with the aid of a separation barrier. A 20-μl biuret reagent reservoir is separated into 5-μl droplets and mixed with 20-μl droplets with bovine albumin at different concentrations. The dashed black arrows represent the synchrotronic motion of the droplet and the acoustic source. The dashed purple circles indicate the initial droplets of clear bovine albumin solution. (**C** to **E**) Liver organoid culture and functional analysis with the SFP. (C) Schematic diagram illustrating mouse liver organoid culturing and functionality characterization. The dashed black arrows represent the synchrotronic motion of the droplet and the acoustic source. The black arrows represent the process flow of the SFP. (D) Immunofluorescent images and fluorescent intensity comparing verapamil's influence on rhodamine 123 localization capability of mouse liver organoids. (E) Immunofluorescent images comparing biliatresone toxicity to liver organoids, where dimethyl sulfoxide (DMSO) and biliatresone with concentrations at 2 and 20 μg ml^{-1} in DMSO are added. The green fluorescence indicates microfilaments F-actin distributions in cytoskeletons, and the blue fluorescence indicates cell nuclei arrangements and distributions. DAPI, 4′,6-diamidino-2-phenylindole. **** indicate P value less than 0.0001, making the fluorescent intensity difference statistically significant. Image credit: H.Z., The University of Hong Kong.

Downloaded from https://www.science.org at Hong Kong Polytechnic University on June 23, 2025

and fig. S19). A statistically significant difference ($P < 0.0001$) in dye accumulation shows that the SFP-cultured organoids exhibit transportation function, while the addition of verapamil inhibits active transportation to luminal space by MDR1. To test the feasibility of the SFP-cultured liver organoids for drug screening, we incubate the organoids with biliatresone at different concentrations (Fig. 5E). Biliatresone can cause biliary atresia, a disease that can result in liver fibrosis for children and associates greatly with the blockage of bile ducts (*53*). After 90 min of incubation in 37°C, while healthy cytoskeleton distribution and nucleus arrangement appear in the control (0 μg ml^{-1}), higher drug concentrations cause destabilization and even mislocation of the cytoskeleton (*54*), demonstrating SFP's utility for cell culture and analysis. Such a damage-free and biocompatible nature endows the SFP with potential for closed-loop microfluidics, where comprehensive fluidic operations are desired without contamination or liquid loss.

DISCUSSION

The spatiotemporal control of acoustic field endows the SFP with a full landscape of microfluidic functions, in a contactless and loss-free manner, including pulling, pushing, merging, separating, and vortexing. A variety of acoustic pressure distributions may empower the acoustic field to achieve more sophisticated fluidic operations and droplet patterning (*55*, *56*), while tailored tuning of the slippery layer may enhance precise processing of specific chemical or biological fluids. Along with its compatibility with liquids of various types and volumes, the SFP works both as a tweezer to move droplet and as a blade to cut droplet on demand, enriching our toolbox for biological/chemical fluidic engineering that demands precision patterning, constructing, printing, and disintegrating multicompartment microdroplets, thus holding substantial importance for various droplet-related applications such as lab-on-a-chip systems, medical diagnosis, and biomedical assays.

MATERIALS AND METHODS

Fabrication of the slippery surface

To prepare hydrophobic silicon dioxide nanoparticles, we mixed 88% (v/v) ethanol absolute (VWR Chemicals), 0.3% (v/v) triethoxy-1*H*,1*H*,2*H*,2*H*-perfluorodecylsilane (98%; ShangFluoro), 0.3% (v/v) tetraethyl orthosilicate (TEOS; 98%; Dieckmann), and 11.4% (v/v) ammonia (25%; AnalaR NORMAPUR), and 0.2% (w/v) silicon dioxide nanoparticles (15 nm, 99.8%; Maikun Chemical) and vigorously stirred overnight under ambient condition in a sealed glassware (*49*). Under an ethanol environment, we added ammonia to catalyze the simultaneous hydrolysis of triethoxy-1*H*,1*H*,2*H*,2*H*-perfluorodecylsilane and TEOS. Subsequently, the condensation reactions on silicon dioxide nanoparticles formed a uniform suspension of hydrophobic polysiloxane/silica nanoparticles.

To fabricate the slippery surface, we sequentially applied three layers of coating: a polymer coating (NeverWet, Rust-Oleum), a silicon dioxide coating, and a fluorinated oil coating (Krytox GPL101, Dupont). We first spray-coated the as-received surface of choice with polymer coating. After 5 min of drying, we spray-coated the prepared silicon dioxide nanoparticle suspension onto the surface under 0.2-MPa nitrogen flow using an airbrush (high performance plus, Iwata). Last, we drop-casted the fluorinated oil onto the surface until a uniform layer was formed.

Acoustic manipulation system

The acoustic manipulation system consisted of a dc power supply (PS5020, Hainan Paisheng Co. Ltd.), a laptop, an Arduino Uno driver board, an L298N driver board, and an ultrasonic sensor (58 kHz; E-sound). The crystal oscillator on the Arduino Uno driver board generateed a stable 58-kHz signal waveform, which the L298N driver board amplified to activate the sensor. We used an oscilloscope to verify the sinusoidal waveform (InfiniVision DSOX4022A, Keysight). Such a combination provided a suitable operational environment for SFP. We also used a custom-built three-axis mechanical linear motion stage to ensure precise control of the droplets.

Contact angle, sliding angle, and contact angle hysteresis

To measure the contact angles, we added 5-μl droplets of acetone (VWR Chemicals), dimethyl sulfoxide (DMSO; 99%; Infinity Scientific), ethanol (RCI Labscan), isopropanol (RCI Labscan), glycerol (99.5%; Sigma-Aldrich), hexadecane (98%; Macklin), dodecane (99%; Aladdin), silicon oil (DC200, Aladdin), mineral oil (Sigma-Aldrich), and deionized water onto the slippery glass surface. We then measured these droplets with an optical contact angle goniometer (OCA 25, Dataphysics). We calculated the contact angle hysteresis by subtracting receding and advancing angle of a 5-μl droplet. We measured the receding and advancing angles using the contact angle goniometer with a 1-ml glass sampler (Hamilton) equipped with a 25-gauge steel blunt-tip needle. To test the sliding angle, we placed a 2.5-μl liquid droplet on the slippery surface, which we then positioned on a micropositioning stage with rotation capabilities.

Surface microstructure and elemental composition

To characterize the microscopic structure and verify elemental composition of the surface, we used scanning electron microscope (SEM; 1530, LEO) and energy-dispersive x-ray spectroscopy (X-Max 50, Oxford Instruments) to image silicon wafer with silicon dioxide and polymer coatings. To obtain cross-sectional information, we carefully broke the coated silicon wafer in liquid nitrogen and then imaged using the aforementioned SEM.

Liver organoid culture and fluorescent imaging

The substrate for organoid culture was fabricated using 3D printed polylactic acid molds as templates to shape PDMS substrates. The PDMS substrate was coated with slippery layer. To mitigate contamination, we treated the specific pathogen–free and PDMS substrates with gamma radiation (Gammacell 3000 Elan) with a central dose of 13,962 centigray before operation in a biosafety cabinet. Mouse primary cholangiocytes (50,000 ml^{-1}) were mixed with Matrigel and transferred onto the substrates. After Matrigel solidification, we added organoid medium [Advanced Dulbecco's modified Eagle's medium/F12 supplemented with 1% penicillin/streptomycin (Invitrogen) as antibiotics]; 1.25 mM *N*-acetylcysteine (Sigma-Aldrich); 25 μM Hepes, 1% N2, and 1% B27 (Gibco); amphotericin B (Gibco); 10 nM gastrin (Sigma-Aldrich); and the growth factors: 5 μM A83.01 (Tocris Bioscience), fibroblast growth factor 10 (100 ng ml^{-1}; PeproTech), forskolin (Tocris Bioscience), hepatocyte growth factor (25 ng ml^{-1}; PeproTech), mouse epidermal growth factor (50 ng ml^{-1}; PeproTech), 10 mM nicotinamide (Sigma-Aldrich), Noggin (25 ng ml^{-1}; PeproTech), R-Spondin 1 (500 ng ml^{-1}; R&D Systems), Wnt3a (100 ng ml^{-1}; R&D Systems), and 10 μM Y27632 (Sigma-Aldrich). After 7 days of cell culture, we stained the organoids in situ with a viability/cytotoxicity kit (LIVE/DEAD, Life Technologies) with the aid of SFP and incubated for 30 min at 37°C. We then observed the organoids in situ via a fluorescent microscope (BX43, Olympus).

To test organoid functionalities, we performed biliatresone (Axon Medchem) dosing and rhodamine 123 transportation experiments. We added biliatresone at concentrations of 0, 2, and 20 μg ml^{-1} in DMSO to the organoids cultured on the slippery substrate for 7 days and incubated in 37°C for 90 min before confocal imaging (LSM 900, Carl Zeiss). In the rhodamine 123 transportation experiment, the organoids cultured on the slippery substrate for 7 days were released from the Matrigel using cold medium. We treated the released organoids with verapamil [10 μM in Dulbecco's phosphate-buffered saline (DPBS)] and incubated them at 37°C for 30 min. After adding rhodamine 123 (100 μM in DPBS) to both treated and untreated organoids under ambient conditions, we used a laser confocal microscopy to observe the transport process immediately. All the confocal fluorescent images were analyzed using Zeiss Zen 3.8.

Simulation

We simulated the distribution of the acoustic pressure amplitude, acceleration amplitude, and flow field using commercial software COMSOL Multiphysics 6.1. We constructed the acoustic structure of the ultrasonic sensor in a cuboid simulation domain containing a liquid droplet (fig. S8). We used the pressure acoustic module and acoustic streaming module for simulation with the following parameters (table S1). To simulate real-world conditions, we set the cuboid domain with

Downloaded from https://www.science.org at Hong Kong Polytechnic University on June 23, 2025

planar wave radiation boundary, the sensor boundary and the bottom of the cuboid domain as acoustic hard boundaries and enabled the emission plate with normal acceleration. We used the vertical movement model to synchronize the relative acceleration, where the acoustic radiation force component in the vertical direction was balanced with the gravitational force and the viscous force of the droplet. We created meshes in the simulation domain by the tetrahedrons with a maximum size of 0.12 λ, where λ represents the ultrasonic wavelength in air, i.e., 5.917 mm.

Supplementary Materials

This PDF file includes:

Supplementary Text
Figs. S1 to S19
Table S1
Legends for movies S1 to S15
References

Other Supplementary Material for this manuscript includes the following:

Movies S1 to S15

REFERENCES AND NOTES

1. A. R. Wheeler, Putting electrowetting to work. *Science* **322**, 539–540 (2008).
2. S. K. Cho, H. Moon, C. J. Kim, Creating, transporting, cutting, and merging liquid droplets by electrowetting-based actuation for digital microfluidic circuits. *J. Microelectromech. Syst.* **12**, 70–80 (2003).
3. J. Li, N. S. Ha, T. Liu, R. M. van Dam, C. J. Kim, Ionic-surfactant-mediated electro-dewetting for digital microfluidics. *Nature* **572**, 507–510 (2019).
4. X. Tang, P. Zhu, Y. Tian, X. Zhou, T. Kong, L. Wang, Mechano-regulated surface for manipulating liquid droplets. *Nat. Commun.* **8**, 14831 (2017).
5. A. Ozcelik, J. Rufo, F. Guo, Y. Gu, P. Li, J. Lata, T. J. Huang, Acoustic tweezers for the life sciences. *Nat. Methods* **15**, 1021–1028 (2018).
6. D. Foresti, M. Nabavi, M. Klingauf, A. Ferrari, D. Poulikakos, Acoustophoretic contactless transport and handling of matter in air. *Proc. Natl. Acad. Sci. U.S.A.* **110**, 12549–12554 (2013).
7. J. Hartmann, M. T. Schür, S. Hardt, Manipulation and control of droplets on surfaces in a homogeneous electric field. *Nat. Commun.* **13**, 289 (2022).
8. X. Yao, Y. Hu, A. Grinthal, T. S. Wong, L. Mahadevan, J. Aizenberg, Adaptive fluid-infused porous films with tunable transparency and wettability. *Nat. Mater.* **12**, 529–534 (2013).
9. S. Jiang, B. Li, J. Zhao, D. Wu, Y. Zhang, Z. Zhao, Y. Zhang, H. Yu, K. Shao, C. Zhang, R. Li, C. Chen, Z. Shen, J. Hu, B. Dong, L. Zhu, J. Li, L. Wang, J. Chu, Y. Hu, Magnetic Janus origami robot for cross-scale droplet omni-manipulation. *Nat. Commun.* **14**, 5455 (2023).
10. Z. Zhao, H. Li, A. Li, L. Liu, L. Xue, Z. Cai, R. Yuan, X. Yu, Y. Song, Two-orders of magnitude enhanced droplet energy harvesting via asymmetrical droplet-electrodes coupling. *Nano Energy* **108**, 108213 (2023).
11. L. Yang, W. Li, J. Lian, H. Zhu, Q. Deng, Y. Zhang, J. Li, X. Yin, L. Wang, Selective directional liquid transport on shoot surfaces of *Crassula muscosa*. *Science* **384**, 1344–1349 (2024).
12. W. Li, X. Tang, L. Wang, Photopyroelectric microfluidics. *Sci. Adv.* **6**, eabc1693 (2020).
13. W. Yu, H. Lin, Y. Wang, X. He, N. Chen, K. Sun, D. Lo, B. Cheng, C. Yeung, J. Tan, D. Di Carlo, S. Emaminejad, A ferrobotic system for automated microfluidic logistics. *Sci. Robot.* **5**, eaba4411 (2020).
14. G. L. Liu, J. Kim, Y. Lu, L. P. Lee, Optofluidic control using photothermal nanoparticles. *Nat. Mater.* **5**, 27–32 (2006).
15. W. Xu, Y. Jin, W. Li, Y. Song, S. Gao, B. Zhang, L. Wang, M. Cui, X. Yan, Z. Wang, Triboelectric wetting for continuous droplet transport. *Sci. Adv.* **8**, eade2085 (2022).
16. J. Sun, L. Zhang, S. Gong, J. Chen, H. Guo, Mechano-driven tribo-electrophoresis enabled human–droplet interaction in 3D space. *Adv. Mater.* **35**, 2305578 (2023).
17. H. Gudapati, M. Dey, I. Ozbolat, A comprehensive review on droplet-based bioprinting: Past, present and future. *Biomaterials* **102**, 20–42 (2016).
18. K. Dholakia, B. W. Drinkwater, M. Ritsch-Marte, Comparing acoustic and optical forces for biomedical research. *Nat. Rev. Phys.* **2**, 480–491 (2020).
19. D. Foresti, K. T. Kroll, R. Amissah, F. Sillani, K. A. Homan, D. Poulikakos, J. A. Lewis, Acoustophoretic printing. *Sci. Adv.* **4**, eaat1659 (2018).
20. J. Li, W. D. Jamieson, P. Dimitriou, W. Xu, P. Rohde, B. Martinac, M. Baker, B. W. Drinkwater, O. K. Castell, D. A. Barrow, Building programmable multicompartment artificial cells incorporating remotely activated protein channels using microfluidics and acoustic levitation. *Nat. Commun.* **13**, 4125 (2022).
21. Y. Koroyasu, T. V. Nguyen, S. Sasaguri, A. Marzo, I. Ezcurdia, Y. Nagata, T. Yamamoto, N. Nomura, T. Hoshi, Y. Ochiai, T. Fushimi, Microfluidic platform using focused ultrasound passing through hydrophobic meshes with jump availability. *PNAS Nexus* **2**, pgad207 (2023).
22. D. J. Collins, C. Devendran, Z. Ma, J. W. Ng, A. Neild, Y. Ai, Acoustic tweezers via sub–time-of-flight regime surface acoustic waves. *Sci. Adv.* **2**, e1600089 (2016).
23. J. Rufo, F. Cai, J. Friend, M. Wiklund, T. J. Huang, Acoustofluidics for biomedical applications. *Nat. Rev. Methods Primers* **2**, 1–21 (2022).
24. Y. Yang, L. Zhang, K. Jin, M. He, W. Wei, X. Chen, Q. Yang, Y. Wang, W. Pang, X. Ren, X. Duan, Self-adaptive virtual microchannel for continuous enrichment and separation of nanoparticles. *Sci. Adv.* **8**, eabn8440 (2022).
25. A. Marzo, S. A. Seah, B. W. Drinkwater, D. R. Sahoo, B. Long, S. Subramanian, Holographic acoustic elements for manipulation of levitated objects. *Nat. Commun.* **6**, 8661 (2015).
26. D. Foresti, D. Poulikakos, Acoustophoretic contactless elevation, orbital transport and spinning of matter in air. *Phys. Rev. Lett.* **112**, 024301 (2014).
27. Z. Yuan, C. Lu, C. Liu, X. Bai, L. Zhao, S. Feng, Y. Liu, Ultrasonic tweezer for multifunctional droplet manipulation. *Sci. Adv.* **9**, eadg2352 (2023).
28. P. Zhang, C. Chen, X. Su, J. Mai, Y. Gu, Z. Tian, H. Zhu, Z. Zhong, H. Fu, S. Yang, K. Chakrabarty, T. J. Huang, Acoustic streaming vortices enable contactless, digital control of droplets. *Sci. Adv.* **6**, eaba0606 (2020).
29. M. Sui, H. Dong, G. Mu, Z. Yang, Y. Ai, J. Zhao, Acoustofluidic tweezers integrated with droplet sensing enable multifunctional closed-loop droplet manipulation. *Adv. Sci.* **12**, 2409394 (2025).
30. T.-S. Wong, S. H. Kang, S. K. Y. Tang, E. J. Smythe, B. D. Hatton, A. Grinthal, J. Aizenberg, Bioinspired self-repairing slippery surfaces with pressure-stable omniphobicity. *Nature* **477**, 443–447 (2011).
31. X. Han, X. Tang, R. Chen, W. Li, P. Zhu, L. Wang, Citrus-peel-like durable slippery surfaces. *Chem. Eng. J.* **420**, 129599 (2021).
32. Y. Zhang, Y. Jiao, C. Li, C. Chen, J. Li, Y. Hu, D. Wu, J. Chu, Bioinspired micro/nanostructured surfaces prepared by femtosecond laser direct writing for multi-functional applications. *Int. J. Extrem. Manuf.* **2**, 032002 (2020).
33. T. Luo, S. Liu, R. Zhou, C. Zhang, D. Chen, Y. Zhan, Q. Hu, X. He, Y. Xie, Z. Huan, W. Gao, R. Li, G. Yuan, Y. Wang, W. Zhou, Contactless acoustic tweezer for droplet manipulation on superhydrophobic surfaces. *Lab Chip* **23**, 3989–4001 (2023).
34. J. Ju, H. Bai, Y. Zheng, T. Zhao, R. Fang, L. Jiang, A multi-structural and multi-functional integrated fog collection system in cactus. *Nat. Commun.* **3**, 1247 (2012).
35. H. Chen, T. Ran, Y. Gan, J. Zhou, Y. Zhang, L. Zhang, D. Zhang, L. Jiang, Ultrafast water harvesting and transport in hierarchical microchannels. *Nat. Mater.* **17**, 935–942 (2018).
36. C. Gao, L. Wang, Y. Lin, J. Li, Y. Liu, X. Li, S. Feng, Y. Zheng, Droplets manipulated on photothermal organogel surfaces. *Adv. Funct. Mater.* **28**, 1803072 (2018).
37. H. Zhan, Y. Xia, Y. Liu, H. Sun, W. Ge, S. Feng, Y. Liu, Sustainable droplet manipulation on ultrafast lubricant self-mediating photothermal slippery surfaces. *Adv. Funct. Mater.* **33**, 2211317 (2023).
38. K. Han, Z. Wang, X. Han, X. Wang, P. Guo, P. Che, L. Heng, L. Jiang, Active manipulation of functional droplets on slippery surface. *Adv. Funct. Mater.* **32**, 2207738 (2022).
39. J. Zhang, X. Wang, Z. Wang, S. Pan, B. Yi, L. Ai, J. Gao, F. Mugele, X. Yao, Wetting ridge assisted programmed magnetic actuation of droplets on ferrofluid-infused surface. *Nat. Commun.* **12**, 7136 (2021).
40. J. Guo, D. Wang, Q. Sun, L. Li, H. Zhao, D. Wang, J. Cui, L. Chen, X. Deng, Omni-liquid droplet manipulation platform. *Adv. Mater. Interfaces* **6**, 1900653 (2019).
41. C. Chen, Z. Huang, Y. Jiao, L. Shi, Y. Zhang, J. Li, C. Li, X. Lv, S. Wu, Y. Hu, W. Zhu, D. Wu, J. Chu, L. Jiang, In situ reversible control between sliding and pinning for diverse liquids under ultra-low voltage. *ACS Nano* **13**, 5742–5752 (2019).
42. I. Swyer, R. Fobel, A. R. Wheeler, Velocity saturation in digital microfluidics. *Langmuir* **35**, 5342–5352 (2019).
43. D. Hu, H. Lai, Y. Liu, X. Luo, Y. Song, D. Zhang, Z. Fan, Z. Xie, Z. Cheng, Self-transportation of superparamagnetic droplets on a magnetic gradient slippery surface with on/off sliding controllability. *ChemPhysChem* **23**, e202200321 (2022).
44. Y. Zhang, J. Li, L. Xiang, J. Wang, T. Wu, Y. Jiao, S. Jiang, C. Li, S. Fan, J. Zhang, H. Wu, Y. Zhang, Y. Bian, K. Zhao, Y. Peng, W. Zhu, J. Li, Y. Hu, D. Wu, J. Chu, Z. Wang, A biocompatible vibration-actuated omni-droplets rectifier with large volume range fabricated by femtosecond laser. *Adv. Mater.* **34**, 2108567 (2022).
45. M. H. Biroun, L. Haworth, P. Agrawal, B. Orme, G. McHale, H. Torun, M. Rahmati, Y. Fu, Surface acoustic waves to control droplet impact onto superhydrophobic and slippery liquid-infused porous surfaces. *ACS Appl. Mater. Interfaces* **13**, 46076–46087 (2021).
46. L. P. Gorkov, Forces acting on a small particle in an acoustic field within an ideal fluid. *Sov. Phys. Dokl.* **6**, 773 (1962).
47. E. A. Neppiras, Acoustic cavitation. *Phys. Rep.* **61**, 159–251 (1980).
48. Z. Tian, Z. Wang, P. Zhang, T. D. Naquin, J. Mai, Y. Wu, S. Yang, Y. Gu, H. Bachman, Y. Liang, Z. Yu, T. J. Huang, Generating multifunctional acoustic tweezers in Petri dishes for contactless, precise manipulation of bioparticles. *Sci. Adv.* **6**, eabb0494 (2020).
49. X. Tang, Y. Tian, X. Tian, W. Li, X. Han, T. Kong, L. Wang, Design of multi-scale textured surfaces for unconventional liquid harnessing. *Mater. Today* **43**, 62–83 (2021).

Downloaded from https://www.science.org at Hong Kong Polytechnic University on June 23, 2025

50. B. Zhang, A. Korolj, B. F. L. Lai, M. Radisic, Advances in organ-on-a-chip engineering. *Nat. Rev. Mater.* **3**, 257–278 (2018).
51. M. J. Kratochvil, A. J. Seymour, T. L. Li, S. P. Paşca, C. J. Kuo, S. C. Heilshorn, Engineered materials for organoid systems. *Nat. Rev. Mater.* **4**, 606–622 (2019).
52. M. Ogawa, S. Ogawa, C. E. Bear, S. Ahmadi, S. Chin, B. Li, M. Grompe, G. Keller, B. M. Kamath, A. Ghanekar, Directed differentiation of cholangiocytes from human pluripotent stem cells. *Nat. Biotechnol.* **33**, 853–861 (2015).
53. J. Li, J. Chu, V. C. H. Lui, S. Chen, Y. Chen, P. K. H. Tam, Bioengineering liver organoids for diseases modelling and transplantation. *Bioengineering* **9**, 796 (2022).
54. O. Waisbourd-Zinman, H. Koh, S. Tsai, P.-M. Lavrut, C. Dang, X. Zhao, M. Pack, J. Cave, M. Hawes, K. A. Koo, J. R. Porter, R. G. Wells, The toxin biliatresone causes mouse extrahepatic cholangiocyte damage and fibrosis through decreased glutathione and SOX17. *Hepatology* **64**, 880 (2016).
55. P. Zhang, T. Li, J. Zhu, X. Zhu, S. Yang, Y. Wang, X. Yin, X. Zhang, Generation of acoustic self-bending and bottle beams by phase engineering. *Nat. Commun.* **5**, 4316 (2014).
56. Y. Guo, B. Li, X. Yin, Dual-compressed photoacoustic single-pixel imaging. *Natl. Sci. Rev.* **10**, nwac058 (2023).
57. D. Daniel, J. V. I. Timonen, R. Li, S. J. Velling, J. Aizenberg, Oleoplaning droplets on lubricated surfaces. *Nat. Phys.* **13**, 1020–1025 (2017).
58. X. Tang, W. Li, L. Wang, Furcated droplet motility on crystalline surfaces. *Nat. Nanotechnol.* **16**, 1106–1112 (2021).
59. X. Chen, R. E. Apfel, Radiation force on a spherical object in an axisymmetric wave field and its application to the calibration of high-frequency transducers. *J. Acoust. Soc. Am.* **99**, 713–724 (1996).

Acknowledgments: We would like to thank N.X. Fang for the equipment support and S. Jiang, J. Lian, X. Wu, S. Xie, B. Yu, and Y. Zhang for discussions. W.L. acknowledges support from Innovation and Technology Commission of Hong Kong though Research Talent Hub (PiH/234/22). X.Y. acknowledges support from the New Cornerstone Science Foundation through the XPLORER Prize and the Hong Kong Jockey Club. H.Z. acknowledges the support from the Research Grants Council of Hong Kong through the Hong Kong PhD Fellowship Scheme. **Funding:** L.W. acknowledges the support from the Research Grants Council of Hong Kong (GRF 17213823, 17205421, and 17204420) and the Hong Kong Polytechnic University (SHS Chair Professor: P0045687). **Author contributions:** L.W., W.L., and H.Z. conceived and designed the project. L.W. and X.Y. supervised the study. H.Z. and W.L. performed the experiments and developed numerical models. Q.D. set up the acoustic devices and motion stage. H.Z., W.L., and L.Y. fabricated and characterized the slippery surfaces. H.Z., H.L., W.L., and C.P. designed and performed microfluidic experiments. J.L. and V.C.-H.L. performed the organoid experiments. H.Z., Q.D., H.L., W.L., Z.W., and Z.Z. analyzed the data. H.Z. wrote the original draft. H.Z., W.L., X.Y., and L.W. revised the manuscript. All authors commented on the paper. **Competing interests:** The authors declare that they have no competing interests. **Data and materials availability:** All data needed to evaluate the conclusions in the paper are present in the paper and/or the Supplementary Materials.

Submitted 30 December 2024
Accepted 31 March 2025
Published 7 May 2025
10.1126/sciadv.adv6314

Downloaded from https://www.science.org at Hong Kong Polytechnic University on June 23, 2025